

RESEARCH ARTICLE

Nanocrystalline-silicon hole contact layers enabling efficiency improvement of silicon heterojunction solar cells: Impact of nanostructure evolution on solar cell performance

Hiroshi Umishio | Hitoshi Sai  | Takashi Koida  | Takuya Matsui 

National Institute of Advanced Industrial Science and Technology (AIST), Tsukuba, Ibaraki, 305-8568, Japan

Correspondence

Takuya Matsui, Global Zero Emission Research Center, National Institute of Advanced Industrial Science and Technology (AIST), Tsukuba, Ibaraki 305-8568, Japan.
Email: t-matsui@aist.go.jp

Funding information

New Energy and Industrial Technology Development Organization (NEDO), Japan

Abstract

Hydrogenated amorphous silicon (a-Si:H) is a key enabler in high-efficiency crystalline silicon solar cells known as the silicon heterojunction technology. Although efforts have been devoted to replacing doped a-Si:H contact layer by hydrogenated nanocrystalline silicon (nc-Si:H) to take advantage of its superior optoelectrical properties, it is still unclear whether the nc-Si:H outperforms the a-Si:H at the high efficiency level. Here, we show that boron-doped (p)nc-Si:H prepared by plasma-enhanced chemical vapor deposition (PECVD) acts as an efficient hole contact layer, providing not only a mitigation of the parasitic absorption loss but also improvements in passivation and electrical contact properties. This results in an efficiency increase by 0.3%–0.6% absolute compared to the reference cell with the (p)a-Si:H, and a best cell efficiency of 23.54%. We find that the critical thickness of the (p)nc-Si:H layers required for gaining high efficiency ($t_c \sim 15\text{--}30\text{ nm}$) is a factor of 3–6 greater than that of the (p)a-Si:H. UV Raman spectroscopy and electrical conductivity measurements reveal that the t_c of the (p)nc-Si:H is associated with the layer growth needing for the surface coalescence of nanocrystals, determining the hole selectivity and the contact resistivity at the electrode/(p)nc-Si:H interface. Our results suggest that such nanostructure evolution can be hastened by using a very-high-frequency PECVD process.

KEYWORDS

amorphous silicon, crystalline silicon, heterojunction, hole selective contact, nanocrystalline silicon, solar cell

1 | INTRODUCTION

Crystalline silicon (c-Si) solar cell is a mainstream technology in today's global photovoltaic market and expected to dominate its share in the next decades, owing to its performance reliability, material abundance, and the recent substantial cost reduction, and so forth. Among various c-Si solar cell technologies, silicon heterojunction (SHJ), which combines c-Si absorber with hydrogenated amorphous silicon (a-Si:H) thin layers, is recognized as one of the device architectures providing the best performance in the laboratory^{1–3} and in the outdoor environment (especially in the hot climate).⁴ Another advantage is the

feasibility for bifacial solar cell module which outperforms the monofacial one in outdoor operation.⁵ However, a drawback of the SHJ solar cells is that the a-Si:H component layers give rise to a non-negligible parasitic optical absorption loss due to its high absorption coefficients in the visible wavelengths. In particular, the incident light absorbed by the doped a-Si:H contact layer does not contribute to any power conversion. It has been reported that only a 5-nm-thick a-Si:H front-contact layer already generates a loss of $\sim 1.5\text{ mA cm}^{-2}$ in photocurrent density.⁶ This negative effect is pronounced in bifacial solar cell, as this type of device allows illumination from both the front and the rear surfaces. Another issue in a-Si:H is its rather high

electrical resistivity, causing a loss in fill factor (FF) especially in the low temperature environment.⁷

Doped hydrogenated nanocrystalline silicon (nc-Si:H) (sometimes referred to as hydrogenated microcrystalline silicon ($\mu\text{c-Si:H}$)) and its alloys, which feature nanometer-sized silicon crystals embedded in an amorphous silicon (alloy) matrix, have attracted attention as an alternative carrier selective contact. This material has been used in high-efficiency thin-film silicon solar cells^{8,9} and implemented into SHJ solar cells as a hole contact^{7,10–15} and an electron contact^{16–24} due to its multifunctionality such as lower parasitic absorption in the visible wavelengths and the better electrical conductivity compared with the doped a-Si:H. Recently, doped nc-Si:H gains more attention for application to a tunneling (recombination) layer between top and bottom cells of perovskite/Si tandem solar cells.^{25,26} However, in a standard single-junction front-rear contacted SHJ architecture, which is the focus of the present study, it is still ambiguous whether the solar cell performance can benefit from the substitution of the conventional a-Si:H by nc-Si:H at the high-efficiency level (>23%). In particular, the use of (p)nc-Si:H as a hole contact of SHJ solar cells is more challenging, as the addition of the *p*-type dopant such as boron (≥ 1 at.%) is prone to hinder the nc-Si:H growth and increase the optical absorption.²⁷ Another challenge is that the thickness of the (p)nc-Si:H (~ 20 – 40 nm) used in the reported SHJ solar cells^{14,15} is substantially thicker than the typical thickness of the (p)a-Si:H (~ 5 nm), which is still a puzzling issue and in fact limits the advantage of its lower optical absorption. Thus, the detailed investigation of the nanostructure evolution of the (p)nc-Si:H in a device-relevant structure is of prime importance. Furthermore, from a viewpoint of industrial application, the fact that deposition rate of nc-Si:H is lower than a-Si:H is also a technical challenge.

In this contribution, we have prepared boron-doped (p)nc-Si:H thin layers by plasma-enhanced chemical vapor deposition (PECVD) using different excitation frequencies (13.56 and 65.0 MHz) and applied them as the front hole contact layers of SHJ solar cells. By implementing (p)nc-Si:H into the well-designed SHJ solar cells, we demonstrate that the (p)nc-Si:H layer enables to improve the solar cell parameters not only short-circuit current density (J_{sc}) but also open-circuit voltage (V_{oc}) and FF, with respect to the reference cell that uses the (p)a-Si:H hole contact layer. In addition, we have studied the growth and electrical properties of the (p)nc-Si:H layers deposited on an intrinsic a-Si:H underlying layer, to correlate their nanostructure

evolution with the solar cell performance. Based on these results, the factors that determine the critical thickness of the (p)nc-Si:H for gaining high V_{oc} and FF are elucidated. An advantage of using a PECVD process operated at higher excitation frequency is proposed to reduce the critical thickness of the (p)nc-Si:H layer as well as to increase the deposition rate.

2 | EXPERIMENTAL

2.1 | Layer deposition and characterizations

The (p)nc-Si:H layers (~ 4 – 40 nm) were deposited by PECVD with a parallel-plate configuration using SiH_4 , B_2H_6 , and H_2 as source gases. In this study, we used two different deposition systems operated at a radio frequency (RF) of 13.56 MHz and at a very high frequency (VHF) of 65.0 MHz. As a reference, the conventional (p)a-Si:H layers were deposited by RF-PECVD. The deposition conditions of these layers (Table I) were individually tuned to attain as high efficiency as possible in our SHJ solar cells.

Planar Si(100) wafers with a thermally grown SiO_2 (30 nm) layer were used to measure the deposited film thickness and crystallinity. Prior to the (p)nc-Si:H deposition, a 10-nm-thick (i)a-Si:H layer was deposited to make a device-equivalent structure, that is, *p-i* layers. In addition, to promote an immediate crystalline nucleation at the (p)nc-Si:H/(i)a-Si:H interface, a CO_2 plasma treatment was applied to the (i)a-Si:H surface for 10–30 s, according to the method reported in Mazzarella et al.¹⁴ Note that this treatment has not been thoroughly studied here and can be replaced by other technique such as hydrogen plasma treatment.²² The deposited layer thickness was characterized by spectroscopic ellipsometry (J.A. Woollam) using the Tauc-Lorentz model. The crystallinity of the (p)nc-Si:H layers was characterized by Raman spectroscopy (Renishaw) using a UV light source (325 nm) generated by He-Cd laser. When measuring UV Raman spectroscopy on very thin (p)nc-Si:H layers (~ 4 nm), the underlying (i)a-Si:H and SiO_2 layers worked effectively in preventing the signal contribution from the c-Si substrate. For electrical characterization, the (p)nc-Si:H/(i)a-Si:H layers stack was deposited on a glass substrate. Coplanar Al contact was formed on top of the (p)nc-Si:H layer to measure the lateral electrical conductivity (Keithley 6430) in a dark shielded box.

TABLE I Deposition parameters of (p)nc-Si:H layers used in VHF-PECVD and RF-PECVD, and those of (p)a-Si:H in RF-PECVD

Material		(p)nc-Si:H	(p)nc-Si:H	(p)a-Si:H
Excitation frequency, MHz		65.0 (VHF)	13.56 (RF)	13.56 (RF)
Gas flow rate	SiH_4 , sccm	3.0	3.5	5.0
	H_2 , sccm	500	700	20
	B_2H_6 , sccm	0.015	0.005	0.075
Pressure, Pa		200	200	66.5
Discharge power density, mW cm^{-2}		347	148	30
Substrate (heater) temperature, $^\circ\text{C}$		180	150	150

Note. The deposition parameters of each hole contact layer were tuned to provide as much efficiency as possible in our SHJ solar cells.

Further sample analysis was carried out by field-emission scanning transmission electron microscopy (TEM) and by secondary-ion mass spectroscopy (SIMS) at Eurofins EAG. Samples for TEM measurements were prepared on glass and *c*-Si substrates for plane-view and cross-sectional observations, respectively. For SIMS measurements, the (*p*)nc-Si:H/(*i*)a-Si:H layers stack was deposited on planar *c*-Si substrate to measure the boron concentration and its distribution in the (*p*)nc-Si:H layers.

2.2 | Solar cell fabrication and characterizations

Phosphorous-doped *n*-type float-zone (FZ) monocrystalline Si wafers (1–3 Ωcm, <100>-oriented) with a thickness of 280 μm were used for solar cell fabrication. For some optimized devices, Czochralski (CZ) wafers featuring thinner thickness (200 μm) were also used. Some wafers were subjected to wet-chemical etching using a KOH-based solution (Hayashi Pure Chemical, Pure Tech) to form random pyramidal textures (average size: ~5 μm) on both surfaces. No additional process was applied for pyramid rounding. After cleaning the wafers, intrinsic (*i*)a-Si:H and *n*-type (*n*)a-Si:H thin layers were successively deposited as passivation and electron contact layers, respectively, on the rear side of solar cells in an RF-PECVD multichamber system using SiH₄, PH₃, and H₂ as source gases. Afterward, the wafers were taken out to flip and immediately loaded back to the same system. Then, the (*i*)a-Si:H was deposited on the front (illumination) side of the wafers. Finally, the *p*-type hole contact layer was deposited in the same manner as described in the previous subsection. For a reference cell, our standard (*p*)a-Si:H was used as a hole contact. Note that for the deposition of the (*p*)nc-Si:H in the VHF-PECVD system, the samples were subjected to a short air break between the depositions of (*i*)a-Si:H and (*p*)nc-Si:H layers. Prior to loading to the VHF-PECVD system, the wafers were HF-dipped to remove the possibly-grown native oxide at the front (*i*)a-Si:H surface. We confirmed that the influence of these additional processes (air break and the following HF-dip) on solar cell performance is negligible, by checking the performance of the SHJ solar cells prepared entirely by RF-PECVD system with an intentional air break at the *p*/*i* interface.

As a result, SHJ cell precursors with a *piNin* structure (here *N* denotes the *n*-type Si wafer) were formed. The details of our PECVD process optimization can be found elsewhere.^{28,29} After the PECVD process, In₂O₃:Sn (ITO) layers and Ag electrodes were sputtered on both sides of the *piNin* structures (through the shadow masks for the front). Prior to Ag sputtering, thermal annealing was performed at 160°C for 2 h in ambient air. No antireflective coating was applied to our solar cells in this study.

The effective minority carrier lifetime of the SHJ cell precursors was monitored at each process step with a quasi-steady-state photoconductance (QSSPC) measurement setup (Sinton Instruments, WCT-120), and the implied V_{oc} (iV_{oc}) was calculated. For the completed cells, the current density-voltage (*J*-*V*) characteristics were measured using a solar simulator under air mass 1.5 global (AM1.5G) and 100 mW cm⁻² illumination at 25°C, and the V_{oc} , the J_{sc} , the FF, and

the conversion efficiency were recorded. The cell area was either 1.12 or 4.32 cm² including Ag-grid, whereas the cell illumination area was 1 or 4 cm² designated by a black shadow mask. All the cells were characterized under illumination from the *p*-layer side. *J*-*V* characteristics of some selected samples were measured by Calibration, Standards and Measurement Team, Research Center for Photovoltaics (currently Photovoltaic Calibration, Standards and Measurement Team, Renewable Energy Research Center) of AIST. External quantum efficiency (EQE) spectra were measured with a Bunkou-Keiki, CEP-25BXS setup.

2.3 | Contact resistivity measurements

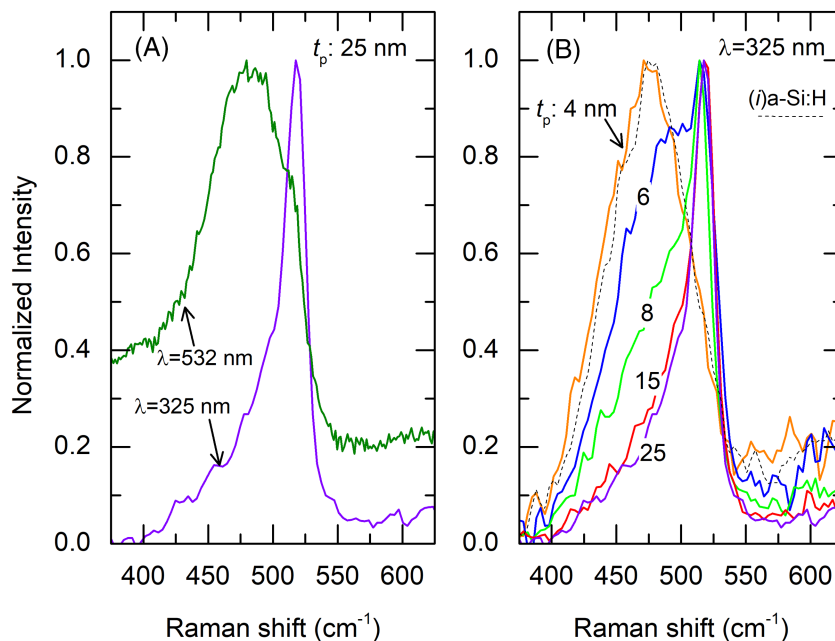
Contact resistivity test structures were fabricated on textured 280-μm-thick 3 Ωcm *p*-type FZ Si wafers. To form an ohmic contact at the single side of the wafer, a 25-nm-thick (*p*)a-Si:H layer (same doping type with the wafer) capped with a sputtered Ag (600 nm) was deposited on the rear side of the wafer.³⁰ The *p*-*i* layers stack under investigation was deposited on the front side of the Si wafer, followed by the sputtered ITO (70 nm) and Ag (3000 nm) pads using shadow masks (8.5 × 13.0 mm² windows for ITO and 8.0 × 12.5 mm² windows for Ag). The contact resistivity of the (*p*)a-Si:H/Ag stack at the rear was evaluated by making a symmetric Ag/(*p*)a-Si:H/(*p*)c-Si/(*p*)a-Si:H/Ag sample. Two-terminal *J*-*V* measurements were performed using a Keithley 6430 source meter.

3 | RESULTS AND DISCUSSION

3.1 | Nanostructure evolution of (*p*)nc-Si:H layers

A series of (*p*)nc-Si:H layers with varying thickness (t_p) in the range from 4 to 40 nm were prepared on a planar SiO₂(20 nm)/Si(100) substrate to evaluate its nanostructure evolution. To make a device-equivalent structure, a 10-nm-thick (*i*)a-Si:H layer was deposited and treated with a following CO₂ plasma prior to the (*p*)nc-Si:H deposition. In Figure 1A, the typical Raman spectra of a 25-nm-thick (*p*)nc-Si:H layer (VHF-PECVD) measured with two different excitation laser wavelengths (UV: 325 nm and VIS: 532 nm) are compared. It is evident that the UV Raman spectroscopy allows to detect a narrow peak appearing at ~520 cm⁻¹ associated with crystalline component, whereas it is hardly detectable with the VIS Raman spectroscopy, but a broad peak associated with amorphous component appears at ~480 cm⁻¹ instead. The UV Raman signal (height and line width) at ~520 cm⁻¹ reflects both the crystalline fraction and the average crystallite size^{31,32} at the film surface no deeper than 5 nm due to the shallow penetration depth of the UV light in Si. This demonstrates an advantage of exploiting the UV Raman spectroscopy particularly for probing such a thin nc-Si:H material. Using the UV Raman spectroscopy, Raman spectra of the (*p*)nc-Si:H layers with different thicknesses were recorded as shown in Figure 1B. By comparing the Raman spectra of the (*p*)nc-Si:H layers with a reference spectrum of the underlying (*i*)a-Si:H layer, the

FIGURE 1 Normalized Raman spectra of (*p*) nc-Si:H layers deposited by VHF-PECVD on a planar substrate consisting of (*i*)a-Si:H (10 nm)/SiO₂(30 nm)/Si(100). A CO₂ plasma treatment was applied on the (*i*)a-Si:H surface prior to the (*p*) nc-Si:H deposition. (A) Comparison of UV ($\lambda = 325$ nm) and VIS ($\lambda = 532$ nm) Raman spectroscopy measurements on a 25-nm-thick (*p*) nc-Si:H layer. Note that for VIS Raman spectroscopy, a glass substrate was used instead of the SiO₂/Si(100) due to the deeper penetration depth of the VIS light in Si (~ 500 nm). (B) UV Raman spectra of the (*p*)nc-Si:H layers with the variation of thickness (t_p) from 4 to 25 nm. The dashed line represents the Raman spectrum of the underlying (*i*)a-Si:H layer [Colour figure can be viewed at wileyonlinelibrary.com]



crystalline nucleation is found to start at a thickness between $t_p = 4$ and 6 nm. With increasing thickness ($t_p \sim 6$ –15 nm), the amorphous component declines while the crystalline component prevails, and the Raman spectrum does not change much when $t_p > 15$ nm.

Figure 2 shows (A) thickness t_p and (B) UV Raman crystallinity I_c/I_a , defined as the ratio of the crystalline peak height I_c at

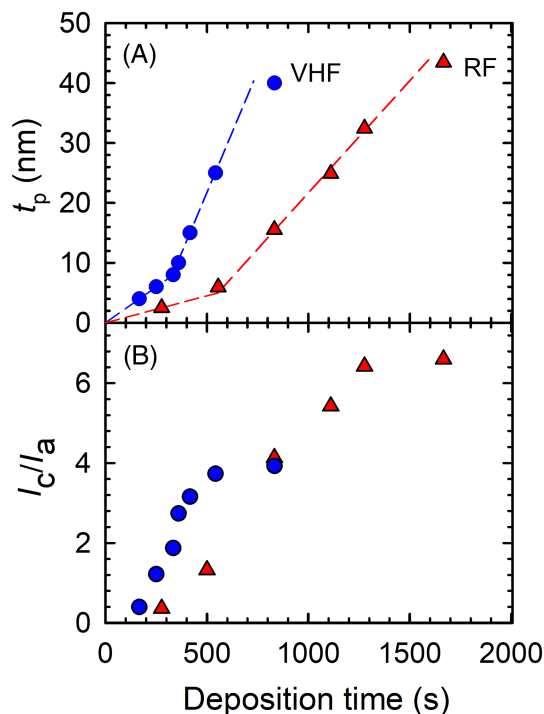


FIGURE 2 (A) Thickness t_p and (B) Raman crystallinity I_c/I_a of the (*p*)nc-Si:H layers as a function of the deposition time of the VHF-PECVD (blue circles) and the RF-PECVD (red triangles) processes. The dashed lines in (A) are the guides to the eyes [Colour figure can be viewed at wileyonlinelibrary.com]

520 cm⁻¹ over the amorphous peak height I_a at 480 cm⁻¹ of the (*p*) nc-Si:H layers, plotted versus the deposition time for the VHF- and the RF-PECVD processes. In Figure 2A, the deposition rate R_d , which is represented by the slope of the thickness-time plot, is higher for VHF-PECVD by a factor of ~ 2 than for RF-PECVD. This can be partly attributed to the increased electron density in VHF plasma and thus to the increased dissociation of the source gas molecules.³³ The higher B₂H₆ doping used in the VHF-PECVD is also a possible reason for the enhanced R_d .^{27,34} It is worth noting that the R_d of the (*p*)nc-Si:H is not constant within the deposition time investigated. At $t_p \sim 8$ nm, we find a notable increase in R_d for VHF-PECVD and a less pronounced increase in R_d for RF-PECVD. By comparing this growth evolution with the Raman crystallinity shown in Figure 2B, the R_d increase can be associated with the growth transition from an amorphous-crystalline mixed state to a crystalline dominant state. In Figure 2B, the I_c/I_a increases abruptly for VHF-PECVD and gradually for RF-PECVD until t_p reaches ~ 15 –25 nm and ~ 25 –30 nm, respectively. The saturation of the I_c/I_a indicates an almost full surface coverage with the crystalline phase because of the high-surface-sensitivity of the UV Raman spectroscopy. This interpretation agrees with the plane-view TEM observation of the (*p*)nc-Si:H layers ($t_p \sim 6, 8,$ and 15 nm by VHF-PECVD) shown in Figure 3. In Figure 3, lattice fringes due to electron beam diffraction are indicated by arrows, which are attributed to the Si nanocrystals whose crystallographic planes are favorably oriented with respect to the electron beam. The lattice fringes observed in the thinnest (*p*)nc-Si:H layer are the manifestation that crystalline nucleation in the amorphous matrix has already started at $t_p \leq 6$ nm. It is seen that the fraction of the lattice fringes increases with t_p , in agreement with the results of the UV Raman spectroscopy measurement. At $t_p \sim 15$ nm, where the material is the onset of the Raman crystallinity saturation, the dark/bright contrast appears markedly. This indicates that a number of randomly

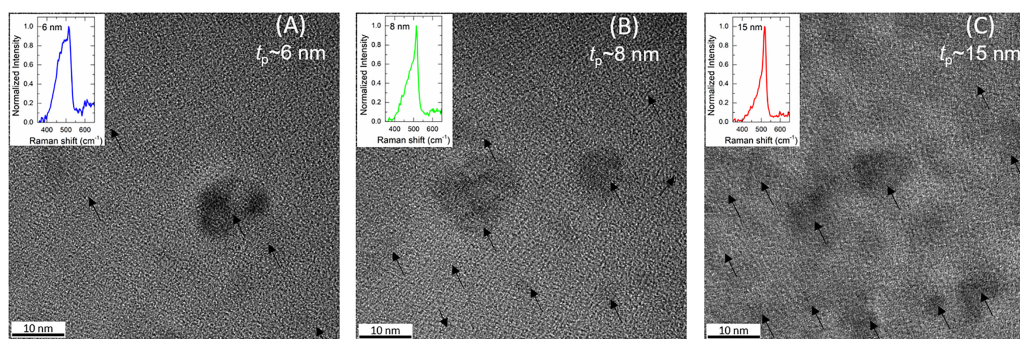


FIGURE 3 Plane-view TEM images of the (p)nc-Si:H layers deposited by VHF-PECVD with the variation of thickness: (A) $t_p \sim 6$ nm, (B) $t_p \sim 8$ nm, and (C) $t_p \sim 15$ nm. These samples consist of a multilayer stack of (i)a-Si:H (5 nm)/(p)nc-Si:H/(i)a-Si:H (10 nm)/glass, where the capping (i)a-Si:H was formed to prevent (p)nc-Si:H from oxidation, while the underlying (i)a-Si:H was to make a device-equivalent structure. Lattice fringes from some of the favorably oriented Si nanocrystals are indicated by the arrows. Insets show the UV Raman spectra of the corresponding layers taken from Figure 1B, which were deposited on a different substrate (SiO_2 (30 nm)/Si(100)) [Colour figure can be viewed at wileyonlinelibrary.com]

distributed nanocrystals with diameters of 5–15 nm are present and start coalescing each other.

Meanwhile, as shown in Figure 2B, the faster saturation and the lower I_c/I_a are observed for the (p)nc-Si:H deposited by VHF-PECVD compared to that by RF-PECVD. It is known that the peak width of the Raman crystalline component reflects the crystalline size if it is in the order of several tenths of nanometers.^{31,32,35} From the measured UV Raman spectra, the full width of the Raman crystalline peak at the half maximum (FWHM) of the ~ 25 nm-thick (p)nc-Si:H deposited by VHF- and RF-PECVD are found to be approximately 20 and 16 cm^{-1} , respectively (not shown). Although the measured UV Raman spectra are broadened due to our spectrometer's resolution, the larger FWHM for the (p)nc-Si:H by VHF-PECVD indicates that it is composed of smaller nanocrystals and this is likely to account for the lower I_c/I_a . Above UV Raman results suggest that VHF-PECVD provides larger density of crystalline nucleation on the (i)a-Si:H surface, which results in a faster coalescence of small crystallites at the (p)nc-Si:H surface.

3.2 | Performance of SHJ solar cells featuring (p)nc-Si:H hole contact layers

The solar cell structure fabricated in this study is shown schematically in Figure 4A. Because the solar cells were made using the textured c-Si, the thickness of the hole contact layer (t_p) on a pyramid-shaped Si {111} facet differs from that on a planar Si(100). Figure 4B,C shows the cross-sectional TEM images of the (p)nc-Si:H/(i)a-Si:H layers stack deposited on textured and planar surfaces, respectively, under the same deposition condition. It is seen that the thicknesses of these layers are thinner for textured Si than for planar substrate due to the larger surface area of the textured Si. We determine the geometrical factor of ~ 1.7 according to their film thickness ratio. Although the actual t_p can be corrected using this geometrical factor, we hereafter use the “nominal t_p ” (uncorrected thickness) when discussing the results of the textured SHJ solar cells.

In Figure 5, solar cell parameters of the SHJ solar cells featuring (p)nc-Si:H (VHF- and RF-PECVD) and (p)a-Si:H (RF-PECVD) hole

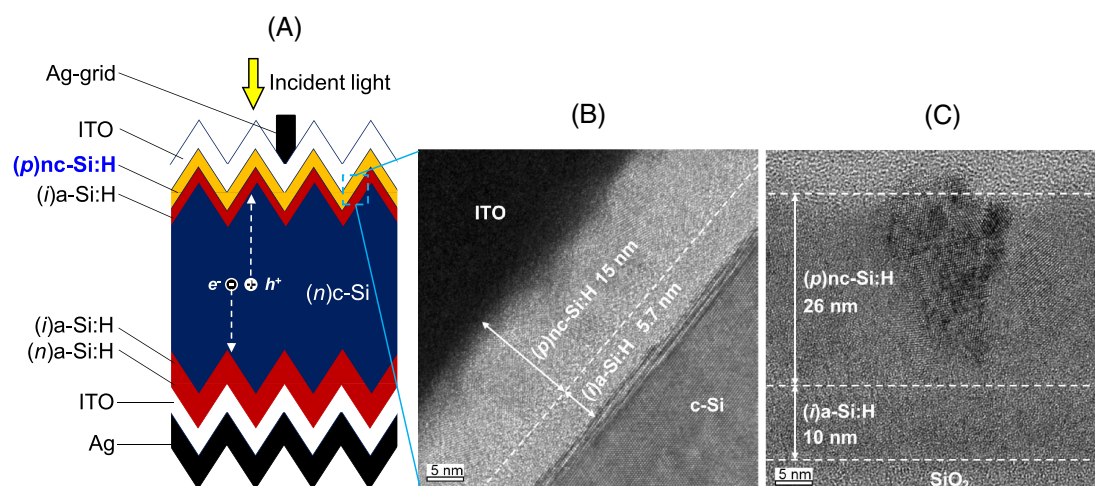
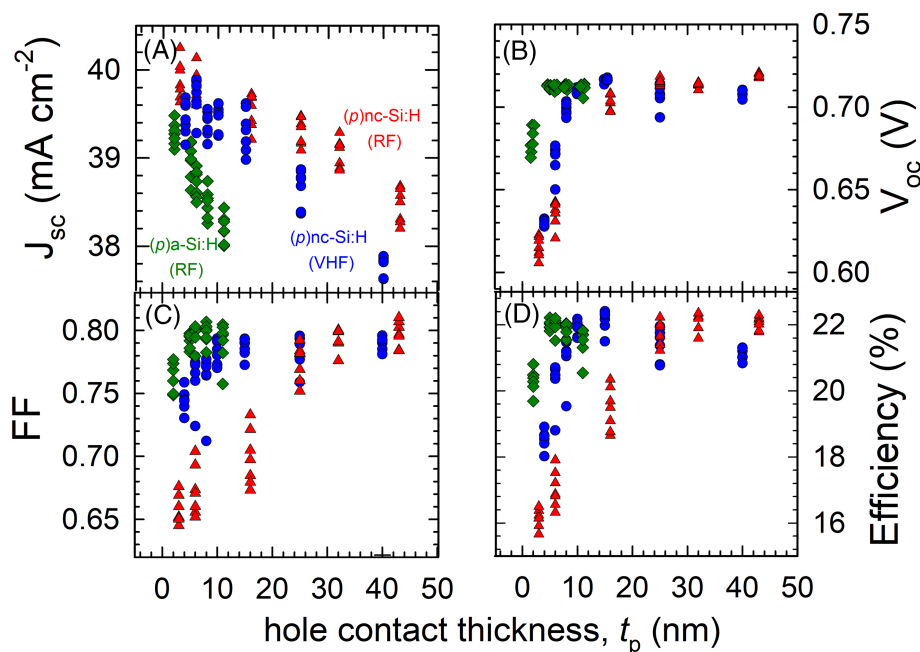


FIGURE 4 (A) Schematic illustration of SHJ solar cell fabricated in this study. (B, C) Cross-sectional TEM images of the (p)nc-Si:H/(i)a-Si:H stacked layers on (B) textured Si (solar cell) and (C) planar substrate, deposited by RF-PECVD under the same condition [Colour figure can be viewed at wileyonlinelibrary.com]

FIGURE 5 J-V parameters of SHJ solar cells featuring (p)nc-Si:H and (p)a-Si:H hole contact layers as a function of their thickness t_p . (A) J_{sc} , (B) V_{oc} , (C) FF, and (D) efficiency. The (p)nc-Si:H layers were deposited by VHF-PECVD (blue circles) and by RF-PECVD (red triangles), and the reference (p)a-Si:H layers were deposited by RF-PECVD (green diamonds). The t_p represents the nominal thickness of the hole contact layers. The rather large spread of J_{sc} and FF comes partly from the different Ag-gird pitches (1.8–2.6 mm) used for seven cells on a substrate. Here, our standard (unoptimized) cell design was employed: a wafer thickness of 280 μm , a device area of 1.0 cm^2 , and an ITO as the front and the rear TCO layers [Colour figure can be viewed at wileyonlinelibrary.com]



contacts are shown as a function of t_p . As shown in Figure 5A, J_{sc} decreases with t_p for any hole contact layers due to the increase of the parasitic absorption loss. However, the J_{sc} decrease is much lower for (p)nc-Si:H than (p)a-Si:H with increasing t_p . This demonstrates an advantage of the (p)nc-Si:H over the (p)a-Si:H in mitigating the parasitic absorption loss. It also appears that the (p)nc-Si:H (RF-PECVD) is more transparent than the (p)nc-Si:H (VHF-PECVD). Although the deposition parameters of the two different deposition systems are difficult to compare, we found an optimum deposition condition at slightly lower deposition temperature and at lower B_2H_6 concentration for RF-PECVD. These deposition strategies are known to provide the lower amorphous volume fraction¹⁵ as well as the lower optical absorption in the amorphous tissue remaining in the (p)nc-Si:H.^{15,27,34} In Figure 5B,C, dependence of V_{oc} and FF on t_p differs significantly between the solar cells with (p)nc-Si:H and (p)a-Si:H. Here, we define the critical thickness of the hole contact layer (t_c) that brings the highest (saturation of) V_{oc} and FF. It is seen that the t_c of (p)a-Si:H is ~ 5 nm, whereas the t_c of (p)nc-Si:H is much thicker and strongly depends on the deposition condition ($t_c \sim 15$ nm for VHF-PECVD and $t_c \sim 25$ –30 nm for RF-PECVD). The thicker t_c of (p)nc-Si:H is an

obstacle in exploiting its less optical absorption properties. In fact, the gain of efficiency by replacing the thin (p)a-Si:H layer with the thicker (p)nc-Si:H layer is rather marginal ($\sim 0.3\%$ absolute), as shown in Figure 5D, due to the tradeoff between J_{sc} and V_{oc} /FF. The mechanism behind the different critical thicknesses found between (p)nc-Si:H and (p)a-Si:H will be discussed in the following subsection.

As shown in Figure 5, the effect of applying the (p)nc-Si:H hole contact layer on solar cell efficiency is not remarkable. However, the advantage of (p)nc-Si:H over (p)a-Si:H appears more clearly when applying them in a well-designed solar cell structure. Table II compares the parameters of solar cells featuring (p)nc-Si:H and (p)a-Si:H hole contact layers prepared by RF-PECVD after improving the cell design other than the PECVD process. Here, we applied a thinner wafer (from 280 μm [FZ-Si] to 200 μm [CZ-Si]) and a larger cell area (from 1.0 to 4.0 cm^2). Both essentially increase the potential V_{oc} , as the former increases the excess carrier density (if the surface recombination is well suppressed by passivation)²⁹ and the latter mitigates the perimeter effect that appears if the device dimension is not large enough compared to the carrier diffusion length.³⁶ As shown in Table II, slightly higher V_{oc} and FF are attained for the solar cell with

TABLE II Summary of the J-V parameters of the best-efficiency SHJ solar cells featuring (p)a-Si:H and (p)nc-Si:H hole contacts

Hole Contact	TCO	Nominal Thickness, nm	J_{sc} , mA cm^{-2}	V_{oc} , V	FF	Efficiency, %
(p)a-Si:H	ITO	5	38.9	0.722	0.801	22.5
(p)nc-Si:H	ITO	25	39.4	0.729	0.804	23.1
(p)a-Si:H	IWOH	5	39.2	0.728	0.805	23.0
(p)nc-Si:H	IWOH	25	39.4	0.730	0.812	23.3
			39.48 ^a	0.733 ^a	0.814 ^a	23.54 ^a

Note. Both hole contact layers were deposited by RF-PECVD. Solar cells were fabricated with an improved cell design, including thinner wafer thickness (200 μm), larger device area (4.0 cm^2), superior TCO layer (IWOH) at the front and the rear.

^aIndependently measured by Calibration and Standard Measurement Team of AIST.

the (p)nc-Si:H hole contact. We found that this comes partly from the improved iV_{oc} (+4 mV), indicating that the passivation of c-Si is enhanced by depositing the (p)nc-Si:H on top of the (i)a-Si:H. We attribute this to the additional supply of atomic hydrogen through the ~ 5 nm-thick (i)a-Si:H underneath layer during the (p)nc-Si:H deposition,¹¹ because the higher hydrogen dilution is used for the (p)nc-Si:H deposition. The much lower deposition rate of the (p)nc-Si:H ($R_d < 0.02$ nm/s) than the (p)a-Si:H ($R_d \sim 0.14$ nm/s) can also play a role in the increased supply of atomic hydrogen. Another beneficial

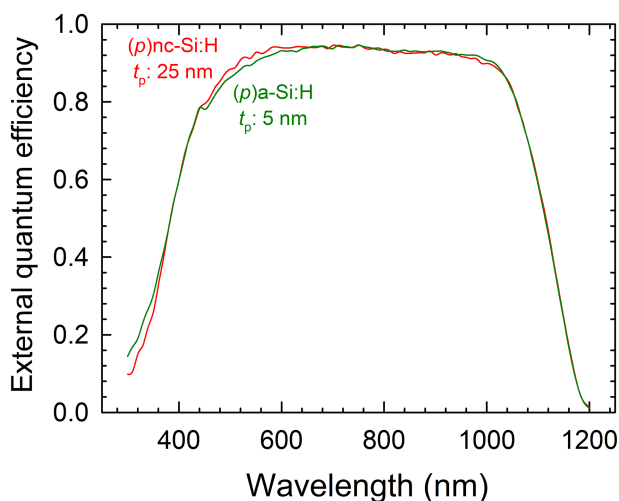


FIGURE 6 EQE spectra of the SHJ solar cells that feature (p)nc-Si:H and (p)a-Si:H hole contact layers deposited at the front side of the solar cells [Colour figure can be viewed at wileyonlinelibrary.com]

effect of using the (p)nc-Si:H hole contact is the reduced contact resistivity at the TCO/p interface, enabling the FF improvement. This will be discussed later in detail.

We emphasize that a J_{sc} gain by 0.5 mA cm^{-2} is still attained, despite the thickness of the (p)nc-Si:H layer is thicker a factor of 5 than that of the (p)a-Si:H. The corresponding EQE spectra shown in Figure 6 demonstrate an improved spectral response in the wavelength range between 500 and 700 nm. The slightly lower EQEs seen in wavelengths of <400 nm can be associated with the increased absorption coefficient because an interband optical transition takes place in the crystalline phase in (p)nc-Si:H. Nevertheless, this loss of EQEs does not affect much on J_{sc} as the number of photons in the AM1.5G spectrum is relatively small in this short wavelength range. As a result of the improved J_{sc} as well as the slight increase in V_{oc} and FF, we attain a 23.1% efficiency. This cell gains 0.6% absolute efficiency compared to our optimized cell that features the standard (p)a-Si:H. Although this efficiency gain is still rather small, this superior performance has been statistically measured for the (unoptimized) SHJ solar cells fabricated in the different batches (Figure 7).

Further cell optimization was carried out by replacing the unoptimized ITO with a tungsten and hydrogen codoped indium oxide (IWOH) layer prepared by the reactive ion plating followed by the solid phase crystallization at a low temperature (160°C).³⁷ As will be discussed later, this allows better electrical contact at the TCO/p interface without sacrificing the optical transparency, leading to a notably high FF above 0.81. As a result, we gain another 0.2% absolute efficiency. The same solar cell was independently measured and

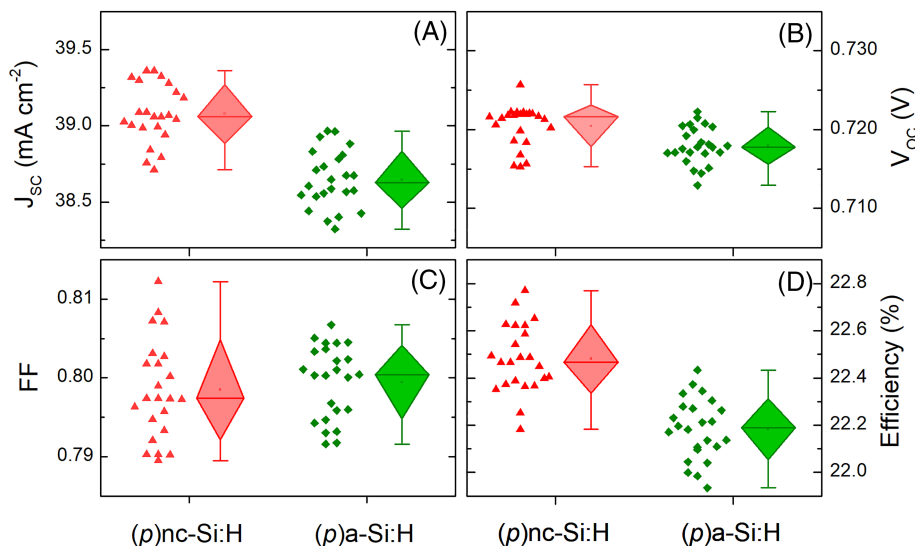


FIGURE 7 J-V parameters of SHJ solar cells with different hole contact layers (red triangles: (p)nc-Si:H (RF-PECVD), $t_p = 25$ nm, green diamonds: (p)a-Si:H (RF-PECVD), $t_p = 5$ nm) fabricated in the multiple batches. (A) J_{sc} , (B) V_{oc} , (C) FF, and (D) efficiency. The boxplots represent the distribution of solar cell parameters. Middle lines and squares correspond to median and mean values, respectively. The height of the box represents 50% of the data, and the whiskers the minimum and the maximum. Solar cells were fabricated using our standard cell design: a wafer thickness of $280 \mu\text{m}$, a device area of 1.0 cm^2 , and an ITO as the front and the rear TCO layers. Note that the spread of J_{sc} and FF comes partly from the different Ag-gird pitches (1.8 – 2.6 mm) used for seven cells on a substrate. The relatively large spread of FF in the samples with the (p)nc-Si:H is due to the thickness/crystallinity inhomogeneity over the substrate, as well as the slight thickness variation of the (p)nc-Si:H layer from batch to batch [Colour figure can be viewed at wileyonlinelibrary.com]

an efficiency of 23.54% was confirmed. The illuminated current-voltage curve of this solar cell is shown in Figure 8.

3.3 | Factors determining the solar cell performance

3.3.1 | Nanostructure evolution of (p)nc-Si:H and its impact on solar cell performance

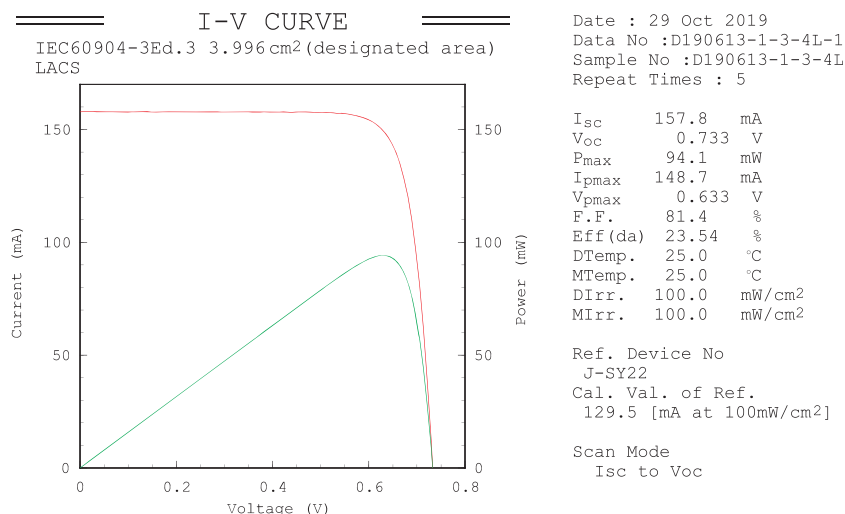
In the previous subsection, we have shown that the efficiency of SHJ solar cells can be improved by replacing the conventional (p)a-Si:H by (p)nc-Si:H. However, the solar cell does not still take full advantage of the lower optical absorption of (p)nc-Si:H, as its critical thickness is rather thick in maximizing V_{oc} and FF. If one could reduce the critical thickness of the (p)nc-Si:H as thin as the (p)a-Si:H, even higher J_{sc} and efficiency can be expected. To elucidate the factors that make the critical thickness of (p)nc-Si:H thicker, we investigated the coplanar conductivity of the (p)nc-Si:H with varying its thickness. Here, we employed a glass substrate to ensure the absence of any dark current contribution via the substrate. To characterize the relevant electrical properties of the (p)nc-Si:H, the (i)a-Si:H deposition on glass and the following CO_2 plasma treatment were performed prior to the (p)nc-Si:H deposition, whereas the (p)a-Si:H was deposited on the (i)a-Si:H without any treatment. In addition, a series of planar SHJ solar cells with varying the thickness of the (p)nc-Si:H hole contact layers (VHF-PECVD) were also prepared, so that the solar cell parameters can be directly compared with the electrical properties and the nanostructure of the (p)nc-Si:H layers that are deposited on planar substrates.

Figure 9 shows the comparison of the (A) coplanar dark conductivity σ_{dark} , (B) UV Raman crystallinity I_c/I_a taken from Figure 2, and (C) V_{oc} and (D) FF of the solar cells, plotted versus t_p for different hole contact materials. In Figure 9A, the σ_{dark} defined here is the electrical conductance of the *p-i* layers stack divided by the *p*-layer thickness. Thus, the measured σ_{dark} is accurate if the σ_{dark} of the *p*-layer is orders of magnitude higher than that of the *i*-layer. The σ_{dark} of the (p)nc-Si:

H layers by VHF- and RF-PECVD varies by 11 and 9 orders of magnitude with increasing t_p , respectively. The σ_{dark} of the thinnest (p)nc-Si:H (~4 nm), where the material exhibits an almost entirely amorphous state, shows values similar to that of the (i)a-Si:H. In contrast, the (p)a-Si:H layer shows higher σ_{dark} by four orders of magnitude although the layer thickness is even thinner (~2 nm). This provides the evidence that the initially-grown (p)nc-Si:H layer (≤ 4 nm) does not act as hole contact at all. With increasing t_p , the σ_{dark} increases abruptly for VHF-PECVD and gradually for RF-PECVD, and it goes far beyond that of the (p)a-Si:H. The slightly higher saturated σ_{dark} observed for the (p)nc-Si:H by VHF- than RF-PECVD is mainly attributed to the different doping concentrations used, as will be shown later. Meanwhile, the higher σ_{dark} of the (p)nc-Si:H ($t_p > 15$ nm) than (p)a-Si:H indicates that the crystalline phase is a dominant electrical conduction path, because both the doping efficiency²⁷ and the hole mobility³⁸ are generally higher for (p)nc-Si:H than for (p)a-Si:H. More importantly, we find an excellent agreement between the changes in electrical conductivity (Figure 9A) and Raman crystallinity (Figure 9B) upon the variation of t_p . In particular, the thicknesses at which the saturation of these parameters occurs are almost the same, indicating that the surface coalescence of nanocrystals increases the number of electrical conduction paths in the lateral direction.

We also find correlations when comparing these material properties of the (p)nc-Si:H layers with the solar cell parameters (V_{oc} and FF). In Figure 9C,D, V_{oc} and FF of the planar solar cells are shown, respectively, along with those of the textured solar cells taken from Figure 5B,C. Here, we note that the deposited layers on planar and textured Si should be different not only in the thickness but strictly speaking also in the material quality. As mentioned earlier, the deposition rate decreases when depositing layers on textured Si, which might particularly affect the nanocrystalline growth. Nevertheless, it is demonstrated that the dependence of V_{oc} on the variation of t_p is almost the same between the planar and the textured solar cells. Although a relatively large difference is found in FF particularly when $t_p \leq 6$ nm, which is mainly due to the thicker (i)a-Si:H layer on planar

FIGURE 8 Current-voltage characteristics of the 23.54% efficient SHJ solar cell featuring (p)nc-Si:H hole contact layer at the front and IWOH layers at the front and the rear, which were independently measured by Calibration, Standards and Measurement Team of Research Center for Photovoltaics (currently Photovoltaic Calibration, Standards and Measurement Team, Renewable Energy Research Center) of AIST [Colour figure can be viewed at wileyonlinelibrary.com]



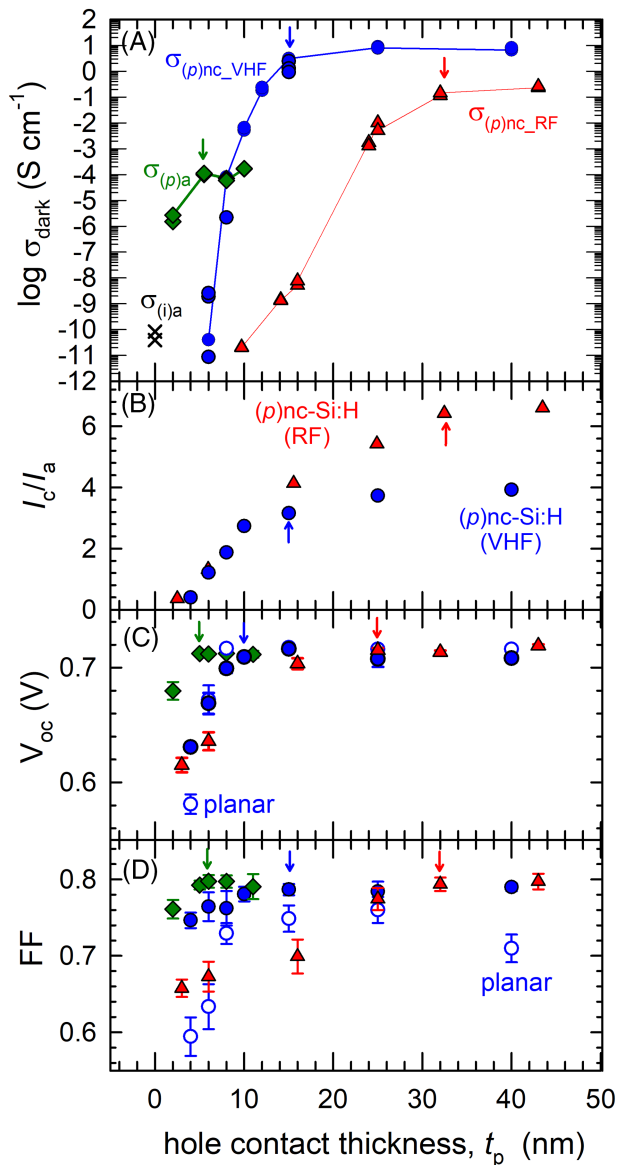


FIGURE 9 Dependence of electrical, structural and solar cell properties on the thickness variation of the hole contact layer (*p*-layer) for different materials including (*p*)nc-Si:H deposited by VHF (blue circles) and by RF-PECVD (red triangles), and (*p*)a-Si:H by RF-PECVD (green diamonds). (A) Coplanar dark conductivity σ_{dark} , (B) UV Raman crystallinity I_c/I_a taken from Figure 2, (C) V_{oc} , and (D) FF of SHJ solar cells. The arrows indicate the thickness at which each parameter is saturated. In (A), the dark conductivity of the underlying (*i*)a-Si:H (10 nm) layer is shown by black crosses. The lines are the guides to the eyes. In (C) and (D), solar cell parameters measured for the planar and the textured *c*-Si absorbers are shown by open and closed symbols, respectively. Error bars represent the spread of the cell parameters over the seven cells fabricated in a same batch. Note that t_p represents the nominal thickness of the hole contact layer [Colour figure can be viewed at wileyonlinelibrary.com]

Si, the t_p that give the highest FF are the same between these solar cells. Thus, we can still relate the material properties of layers deposited on planar substrate with the parameters of the textured solar cells. Here, we redefine the critical thicknesses of the hole contact layers for V_{oc} and FF as $t_{c,V_{\text{oc}}}$ and $t_{c,FF}$, respectively, where the

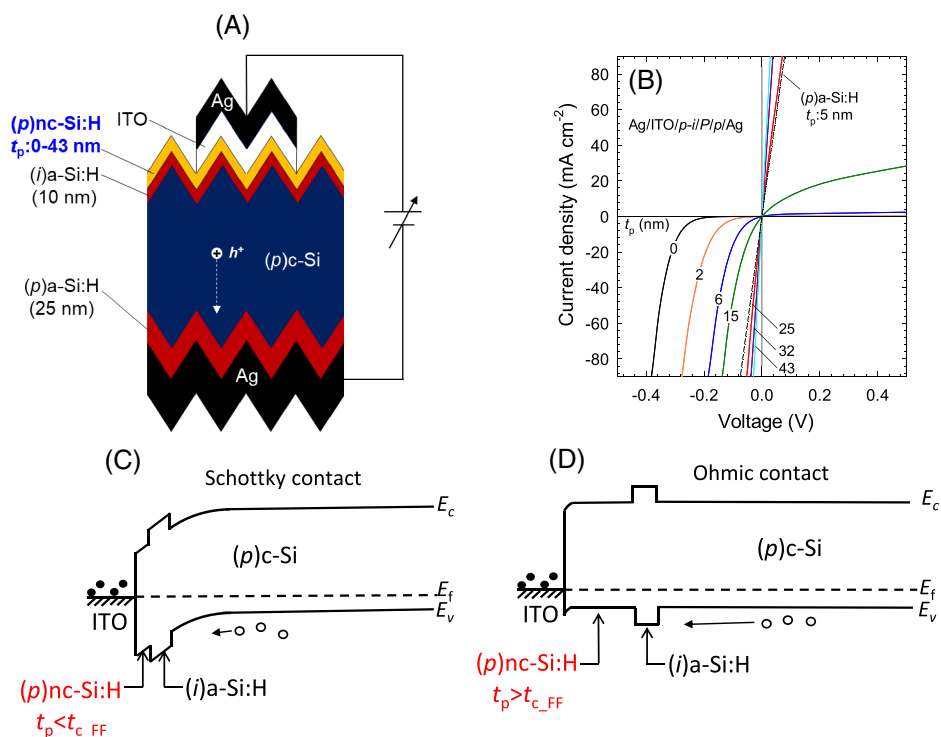
saturation of these parameters occurs. Basically, they are close each other, but to be more precise, the $t_{c,V_{\text{oc}}}$ is slightly thinner than the $t_{c,FF}$. The $t_{c,V_{\text{oc}}}$ is found where the σ_{dark} of the (*p*)nc-Si:H is as high as that of the (*p*)a-Si:H, and where the I_c/I_a is the onset of its saturation. As the measured iV_{oc} (~ 720 mV) is almost independent of the t_p (not shown here), the V_{oc} is governed by the hole selectivity of the contact layers but not by the passivation quality. It has been reported that the *c*-Si band bending induced by the work function difference between the *c*-Si and the contact layer plays a major role in carrier selectivity.³⁹ The density of fixed charge in a-Si:H is negligibly low.⁴⁰ Thus, it is considered that the σ_{dark} of $>10^{-4}$ S cm⁻¹ is high enough to have sufficient hole concentration in the (*p*)nc-Si:H layer in preventing hole contact layer from being depleted after depositing the top electrode (TCO) on it, which is essential to create induced-band bending in the (*n*)c-Si absorber.³⁹

In contrast, $t_{c,FF}$ is found where the (*p*)nc-Si:H layer shows the highest σ_{dark} and where the I_c/I_a is being saturated with respect to the increase of t_p . If the (*p*)nc-Si:H thickness is much thinner than $t_{c,FF}$, an S-shaped J-V curve appeared, indicating that a Schottky diode component builds up at the TCO/*p* interface.^{39,41} By comparing Figure 9A,D, it is found that $t_{c,FF}$ is not directly governed by the conductivity (hole concentration) of the hole contact layer, as the (*p*)a-Si:H provides FF of >0.8 whereas its dark conductivity (10^{-4} S cm⁻¹) is far below the highest one of the (*p*)nc-Si:H ($>10^{-1}$ S cm⁻¹). Therefore, we conclude that the $t_{c,FF}$ is dominated by the surface coverage of the crystalline nanocrystals rather than the electrical conductivity (hole concentration) itself. In other words, the direct electrical contact between the TCO and the remaining amorphous phase at the surface of the (*p*)nc-Si:H results in a creation of the Schottky diode component at the TCO/*p* interface.

3.3.2 | Electrical contact properties at the TCO/*p* interface

The above interpretation on the TCO/*p* contact properties is evidenced by measuring the vertical hole transport using a test structure shown in Figure 10A.³⁰ Figure 10B shows the dark J-V characteristics of the test structure with the thickness variation of the (*p*)nc-Si:H layer deposited by RF-PECVD. A nonlinear J-V behavior is observed when $t_p < t_{c,FF}$ (~ 25 – 30 nm for RF-PECVD), and this trend becomes pronounced as the t_p decreases. This indicates that an undesirable induced-band bending is created in the (*p*)c-Si due to the depletion of the hole contact layer. As mentioned earlier, this is caused by the poor coverage of crystalline phase at the (*p*)nc-Si:H surface and thus by the direct contact between the poorly-conductive amorphous phase and the overlying ITO. On the other hand, an ideal ohmic contact is obtained when $t_p \geq t_{c,FF}$ because the highly conductive crystalline phase and ITO are contacted. These t_p -dependent hole transport properties are in line with the variation of FF shown in Figure 9D (red triangles). We estimate that the average vertical resistivities of the ITO/*p*-*i*/*P* stacked layers are 360 and 520 m Ω cm² at room temperature for the (*p*)nc-Si:H ($t_p = 25$ nm) and the (*p*)a-Si:H ($t_p = 5$ nm),

FIGURE 10 (A) A test structure used for the vertical hole transport measurement. (B) J-V characteristics of the test structure with varying the thickness of the (p)nc-Si:H hole contact layer (t_p) (solid lines). The result when using the (p)a-Si:H is also shown (dashed line). Note that t_p represents the nominal thickness. Possible band diagrams of the ITO/(p)nc-Si:H/(i)a-Si:H/(p)c-Si contact systems that explain (C) nonohmic ($t_p \lesssim 25$ nm) and (D) ohmic ($t_p \gtrsim 32$ nm) behaviors [Colour figure can be viewed at wileyonlinelibrary.com]



respectively. This provides the support that the nc-Si:H performs better than a-Si:H in reducing the contact resistivity at the TCO/p interface.

A replacement of ITO with IWOH effectively lowers the resistivity to 280 and 420 m Ω cm² for both the (p)nc-Si:H ($t_p = 25$ nm) and the (p)a-Si:H ($t_p = 5$ nm) layers respectively, explaining the notable improvement in FF as shown in Table II. We tentatively ascribe the higher contact resistivity for the ITO to a thicker SiO_x interface layer formed during ITO deposition and subsequent postannealing. Here, we used an ITO target with a SnO₂ content of 10 wt.%. To minimize free carrier absorption within the ITO layer, we used an oxygen-rich condition to compensate free carriers by excess oxygen atoms, which might in turn result in the thicker SiO_x interface layer. We believe that there is still room for further optimization of our standard ITO layers by reducing the Sn content.

Above measured resistivities are still an order of magnitude higher in comparison with the ideal values predicted by the theoretical work.⁴² However, this gap might come partly from the presence of

the highly-resistive (i)a-Si:H layer³⁰ and the actual resistivity under cell operation can be lowered by illumination.

3.3.3 | Dopant concentration in (p)nc-Si:H

Meanwhile, it is still unclear why the thin (p)nc-Si:H layers ($t_p \lesssim 10$ nm) are poorly conductive compared to the (p)a-Si:H. To gain insight into this origin, SIMS measurement was performed on the (p)nc-Si:H and the (p)a-Si:H layers. The samples consist of p(5–25 nm)-i(10 nm) layers stack on a planar (n)c-Si substrate. It is found that the peak boron concentrations in the (p)nc-Si:H layers are 2×10^{20} and 6×10^{19} cm⁻³ for VHF-PECVD and RF-PECVD, respectively, whereas that in the (p)a-Si:H by RF-PECVD is 1.0×10^{21} cm⁻³. For the (p)nc-Si:H deposited by RF-PECVD, we confirmed that the peak boron concentration does not change with the thickness variation in the range from 5–25 nm. In Table III, the boron concentrations in the gas-phase C_{B-gas} and that in the solid phase $C_{B-solid}$ are compared. In addition to the standard

TABLE III Comparison of the gas-phase (C_{B-gas}) and the solid-phase ($C_{B-solid}$) boron concentrations in (p)nc-Si:H layers deposited by VHF- and RF-PECVD, and in (p)a-Si:H layers by RF-PECVD

	(p)nc-Si:H (VHF)	(p)nc-Si:H (RF)	(p)a-Si:H (RF) standard	(p)a-Si:H (RF) [B_2H_6] $\times 1/10$
C_{B-gas} , %	1.0	0.28	3.0	0.3
$C_{B-solid}$, %	0.4	0.12	2.4	0.25
σ_{dark} , S cm ⁻¹	4.2×10^{-10} ($t_p \sim 6$ nm)	1.0×10^{-11} ($t_p \sim 10$ nm)	3.8×10^{-5} ($t_p \sim 5$ nm)	4.2×10^{-9} ($t_p \sim 4$ nm)

Note. A (p)a-Si:H layer with a reduced B_2H_6 flux ($\times 1/10$) was also prepared and analyzed for the verification of the SIMS measurement. A Si atom density of 5.0×10^{22} cm⁻³ was assumed for calculating the $C_{B-solid}$ for both the (p)nc-Si:H and the (p)a-Si:H. The typical dark conductivities of these materials with thin thicknesses ($t_p \leq 10$ nm) are also shown.

(p)a-Si:H, another (p)a-Si:H layer with a lower B₂H₆ flux ($\times 1/10$) was also prepared for the verification of the SIMS measurement. In Table III, the C_{B-solid} in the (p)nc-Si:H is about one order of magnitude lower than that in the standard (p)a-Si:H, because the less dopant is required in (p)nc-Si:H due to the higher doping efficiency. Thus, the C_{B-solid} is too small to generate enough free holes in the initially-grown amorphous-rich incubation zone of the (p)nc-Si:H layers. Another finding is that the C_{B-solid} is about a factor of 2 lower than the C_{B-gas} in the (p)nc-Si:H, whereas the C_{B-gas} and the C_{B-solid} are nearly the same in the case of the (p)a-Si:H. This indicates that the boron incorporation efficiency is lower under the (p)nc-Si:H deposition condition, which makes doping into the initial growth region more difficult. Moreover, it is also found from Table III that the σ_{dark} is substantially lower for the thin (p)nc-Si:H layers than for the (p)a-Si:H, even if the C_{B-solid} are comparable. As a possible reason, the dopant inactivation by hydrogen passivation⁴³ and/or bandgap widening might occur due to the high flux of atomic hydrogen during the deposition, which can also account for the poorer conductivity of the amorphous-rich (p)nc-Si:H ($t_p < 10$ nm) layers than that of the standard (p)a-Si:H. These factors are responsible for the low lateral/vertical hole conductivity and for the poor solar cell parameters (V_{oc} and FF) when the thickness of the (p)nc-Si:H is thinner than the critical thickness ($t_{c,V_{\text{oc}}}$ and $t_{c,FF}$), as shown in Figures 9 and 10.

3.4 | Outlook for further improvement and industrial application

Finally, we address the remaining issues regarding the nc-Si:H contact materials for SHJ cell application. In this study we focused on the (p) nc-Si:H material without alloying. Alloying nc-Si:H with oxygen^{10,13,18–24} and carbon¹⁶ is a possible way of further mitigation of the parasitic absorption loss. However, the mixing such as CO₂⁴⁴ and CH₄⁴⁵ gases during the PECVD process generally hampers the nucleation and the growth of nc-Si:H, particularly when doped with the p-type dopant. This makes critical thickness even thicker, which might result in the minor improvement of solar cell efficiency. On the other hand, alloying oxygen in (n)nc-Si:H (i.e., (n)nc-SiO_x:H) has been reported to provide clear advantage in improving J_{sc} and efficiency,²³ as the critical thickness of the (n)nc-SiO_x:H (<10 nm)¹⁹ can be made thinner than that of the (p)nc-Si:H (15–30 nm). This manifests the easier growth of the n-type nc-Si:H and its alloys compared to the p-type counterparts in the conventional PECVD process.

Regarding the deposition method, our results suggest that the use of the VHF plasma source can make the deposition faster and the critical thickness thinner, due to the several beneficial effects including the efficient gas decomposition, the enhanced nucleation, and the immediate coalescence of nanocrystals. The deposition of the alloyed (p)nc-Si:H materials by VHF-PECVD is also a subject worth investigating in the future. Currently, VHF plasma source is not commonly used in the SHJ solar cell production because of the standing wave phenomenon that makes nonuniform plasma distribution over the large area. However, this technological issue has been overcome in the

production of thin-film silicon solar cells and modules.⁴⁶ Thus, VHF-PECVD is still an attractive avenue in industrial application.

4 | CONCLUSIONS

In this work, boron-doped (p)nc-Si:H thin layers have been grown by VHF- and RF-PECVD and applied as front hole contact (emitter) layers of front-rear contacted SHJ solar cells. Although the critical thickness of the (p)nc-Si:H is a factor of 3–6 thicker than that of the (p)a-Si:H, we demonstrate not only an increase in J_{sc} due to the mitigation of the parasitic absorption loss but also increase in V_{oc} and FF thanks to the improved passivation and electrical contact properties. As a result, we attain an efficiency increase by 0.3%–0.6% absolute compared to our reference cell with the (p)a-Si:H. An implementation of the improved TCO material (IWOH) leads to an independently confirmed best cell efficiency of 23.54% (23.3% by in-house measurement). To elucidate the mechanism behind the strong dependence of the V_{oc} and FF on the (p)nc-Si:H thickness, we have characterized a device-equivalent (p)nc-Si:H/(i)a-Si:H layers stack by means of UV Raman spectroscopy, TEM and electrical conductivity. As a result, we find a clear correlation among the nanostructure evolution, lateral/vertical hole conductivity, and the performance of both the textured and the planar solar cells upon the variation of (p)nc-Si:H thickness from 4 to 40 nm. Based on this, we conclude that the surface coverage of the nanocrystals of the (p)nc-Si:H layer, which influences the hole selectivity and the hole transport through the TCO/p interface, is a crucial factor determining the solar cell's V_{oc} and FF. We propose to take advantage of the VHF-PECVD technique for making the faster deposition and the thinner (p) nc-Si:H layer requirement, aiming for industrial application.

ACKNOWLEDGEMENTS

We are grateful to T. Oku, Y. Sato, and M. Tanabe for the technical assistance in wafer preparation, cell fabrication, and characterization and to T. Ueda and M. Yoshita in CSMT-RCPV of AIST for the high-fidelity J-V measurements. We thank P-L. Chen for cooperating on the research and development of the nc-Si:H materials for SHJ solar cell application during her stay in AIST. We also thank T. Kawatsu and T. Nagai of Komatsu NTC Ltd. for providing high-quality CZ-Si wafers and A. Terakawa, M. Matsumoto, T. Hashiguchi, and H. Katayama of Panasonic corporation for fruitful discussion. This work was supported by the New Energy and Industrial Technology Development Organization (NEDO), Japan.

ORCID

Hitoshi Sai  <https://orcid.org/0000-0002-2938-551X>

Takashi Koida  <https://orcid.org/0000-0001-8496-9166>

Takuya Matsui  <https://orcid.org/0000-0003-1589-7052>

REFERENCES

1. Taguchi M, Yano A, Tohoda S, et al. 24.7% record efficiency HIT solar cell on thin silicon wafer. *IEEE J Photovolt*. 2014;4:96–99. <https://doi.org/10.1109/JPHOTOV.2013.2282737>

2. Adachi D, Hernández JL, Yamamoto K. Impact of carrier recombination on fill factor for large area heterojunction crystalline silicon solar cell with 25.1% efficiency. *Appl Phys Lett*. 2015;107(23):1-3, 233506. <https://doi.org/10.1063/1.4937224>
3. Yoshikawa K, Kawasaki H, Yoshida W, et al. Silicon heterojunction solar cell with interdigitated back contacts for a photoconversion efficiency over 26%. *Nat Energy*. 2017;2(5):1-8, 17032. <https://doi.org/10.1038/nenergy.2017.32>
4. Haschke J, Seif JP, Riesen Y, et al. The impact of silicon solar cell architecture and cell interconnection on energy yield in hot & sunny climates. *Energ Environ Sci*. 2017;10(5):1196-1206. <https://doi.org/10.1039/C7EE00286F>
5. Guerrero-Lemus R, Vega R, Kim T, Kimm A, Shephard LE. Bifacial solar photovoltaics—a technology review. *Renew Sustain Energy Rev*. 2019;60:1533-1549. <https://doi.org/10.1016/j.rser.2016.03.041>
6. Holman ZC, Descoedres A, Barraud L, et al. Current losses at the front of silicon heterojunction solar cells. *IEEE J Photovolt*. 2012;2(1):7-15. <https://doi.org/10.1109/JPHOTOV.2011.2174967>
7. Nogay G, Seif JP, Riesen Y, et al. Nanocrystalline silicon carrier collectors for silicon heterojunction solar cells and impact on low-temperature device characteristics. *IEEE J Photovolt*. 2016;6:1654-1662. <https://doi.org/10.1109/JPHOTOV.2016.2604574>
8. Shah A, Meier J, Vallat-Sauvain E, et al. Material and solar cell research in microcrystalline silicon. *Sol Energy Mater sol Cells*. 2003;78:469-491. [https://doi.org/10.1016/S0927-0248\(02\)00448-8](https://doi.org/10.1016/S0927-0248(02)00448-8)
9. Sai H, Matsui T, Matsubara K. Stabilized 14.0%-efficient triple-junction thin-film silicon solar cell. *Appl Phys Lett*. 2016;109(18):1-5, 183506. <https://doi.org/10.1063/1.4966996>
10. Sritharathikhun J, Jiang FH, Miyajima S, Yamada A, Konagai M. Optimization of p-type hydrogenated microcrystalline silicon oxide window layer for high-efficiency crystalline silicon heterojunction solar cells. *Jpn J Appl Phys*. 2009;48:1-5, 101603. <https://doi.org/10.1143/JJAP.48.101603>
11. Ghahfarokhi OM, von Maydell K, Agert C. Enhanced passivation at amorphous/crystalline silicon interface and suppressed Schottky barrier by deposition of microcrystalline silicon emitter layer in silicon heterojunction solar cells. *Appl Phys Lett*. 2014;104(11):1-5, 113901. <https://doi.org/10.1063/1.4868726>
12. Seif JP, Descoedres A, Nogay G, et al. Strategies for doped nanocrystalline silicon integration in silicon heterojunction solar cells. *IEEE J Photovoltaics*. 2016;6(5):1132-1140. <https://doi.org/10.1109/JPHOTOV.2016.2571619>
13. Mazzarella L, Kirner S, Stannowski B, Korte L, Rech B, Schlattmann R. P-type microcrystalline silicon oxide emitter for silicon heterojunction solar cells allowing current densities above 40 mA/cm². *Appl Phys Lett*. 2015;106(2):1-5, 023902. <https://doi.org/10.1063/1.4905906>
14. Mazzarella L, Kirner S, Gabriel O, et al. Nanocrystalline silicon emitter optimization for Si-HJ solar cells: substrate selectivity and CO₂ plasma treatment effect. *Phys Status Solidi*. 2017;214(2):1-7, 1532958. <https://doi.org/10.1002/pssa.201532958>
15. Fioretti AN, Boccard M, Monnard R, Ballif C. Low-temperature p-type microcrystalline silicon as carrier selective contact for silicon heterojunction solar cells. *IEEE J Photovolt*. 2019;9:1158-1165. <https://doi.org/10.1109/JPHOTOV.2019.2917550>
16. Miyajima S, Irikawa J, Yamada A, Konagai M. High-quality nanocrystalline cubic silicon carbide emitter for crystalline silicon heterojunction solar cells. *Appl Phys Lett*. 2010;97:1-3, 023504. <https://doi.org/10.1063/1.3460917>
17. Watahiki T, Furuhashi T, Matsuura T, et al. Rear-emitter Si heterojunction solar cells with over 23% efficiency. *Appl Phys Express*. 2015;8(2):1-3, 021402. <https://doi.org/10.7567/APEX.8.021402>
18. Kim S, Park J, Phong PD, Shin C, Iftiqar SM, Yi J. Improving the efficiency of rear emitter silicon solar cell using an optimized n-type silicon oxide front surface field layer. *Sci Rep*. 2018;8(1):1-10, 10657. <https://doi.org/10.1038/s41598-018-28823-x>
19. Mazzarella L, Morales-Vilches AB, Korte L, Schlattmann R, Stannowski B. Ultra-thin nanocrystalline n-type silicon oxide front contact layers for rear-emitter silicon heterojunction solar cells. *Sol Energy Mater sol Cells*. 2018;179:386-391. <https://doi.org/10.1016/j.solmat.2018.01.034>
20. Mazzarella L, Morales-Vilches AB, Hendrichs M, et al. Nanocrystalline n-type silicon oxide front contacts for silicon heterojunction solar cells: photocurrent enhancement on planar and textured substrates. *IEEE J Photovolt*. 2018;8:70-78. <https://doi.org/10.1109/JPHOTOV.2017.2770164>
21. Morales-Vilches AB, Cruz A, Pingel S, et al. ITO-free silicon Heterojunction solar cells with ZnO:Al/SiO₂ front electrodes reaching a conversion efficiency of 23%. *IEEE J Photovolt*. 2019;9:34-39. <https://doi.org/10.1109/JPHOTOV.2018.2873307>
22. Zhao Y, Mazzarella L, Procel P, et al. Doped hydrogenated nanocrystalline silicon oxide layers for high-efficiency c-Si heterojunction solar cells. *Prog Photovolt Res Appl*. 2020;28:425-435. <https://doi.org/10.1002/pip.3256>
23. Lei C, Peng C-W, Zhong J, et al. Phosphorus treatment to promote crystallinity of the microcrystalline silicon front contact layers for highly efficient heterojunction solar cells. *Sol Energy Mater sol Cells*. 2020;209:1-6, 110439. <https://doi.org/10.1016/j.solmat.2020.110439>
24. Qiu D, Duan W, Lambert A, et al. Front contact optimization for rear-junction SHJ solar cells with ultra-thin n-type nanocrystalline silicon oxide. *Sol Energy Mater sol Cells*. 2020;209:1-7, 110471. <https://doi.org/10.1016/j.solmat.2020.110471>
25. Sahli F, Werner J, Kamino BA, Brauninger M, et al. Fully textured monolithic perovskite/silicon tandem solar cells with 25.2% power conversion efficiency. *Nat Mater*. 2018;17(9):820-826. <https://doi.org/10.1038/s41563-018-0115-4>
26. Jošt M, Kohnen E, Morales-Vilches AB, Lipovsek B, et al. Textured interfaces in monolithic perovskite/silicon tandem solar cells: advanced light management for improved efficiency and energy yield. *Energ Environ Sci*. 2018;11(12):3511-3523. <https://doi.org/10.1039/c8ee02469c>
27. Matsui T, Kondo M, Matsuda A. Doping properties of boron-doped microcrystalline silicon from B₂H₆ and BF₃: material properties and solar cell performance. *J Non Cryst Solids*. 2004;338:646-650. <https://doi.org/10.1016/j.jnoncrysol.2004.03.073>
28. Sai H, Chen PW, Hsu HJ, Matsui T, Nunomura S, Matsubara K. Impact of intrinsic amorphous silicon bilayers in silicon heterojunction solar cells. *J Appl Phys*. 2018;124(10):1-11, 103102. <https://doi.org/10.1063/1.5045155>
29. Sai H, Oku T, Sato Y, Tanabe M, Matsui T, Matsubara K. Potential of very thin and high-efficiency silicon heterojunction solar cells. *Prog Photovolt Res Appl*. 2019;27(12):1061-1070. <https://doi.org/10.1002/pip.3181>
30. Luderer C, Messmer C, Hermlé M, Bivour M. Transport losses at the TCO/a-Si:H/c-Si heterojunction: influence of different layers and annealing. *IEEE J Photovolt*. 2020;10:952-958. <https://doi.org/10.1109/JPHOTOV.2020.2983989>
31. Iqbal Z, Vepřek S, Webb AP, Capezzuto P. Raman scattering from small particle size polycrystalline silicon. *Solid State Commun*. 1981;37(12):993-996. [https://doi.org/10.1016/0038-1098\(81\)91202-3](https://doi.org/10.1016/0038-1098(81)91202-3)
32. Smit C, van Swaaij RACMM, Donker H, Petit AMHN, Kessels WMM, van de Sanden MCM. Determining the material structure of microcrystalline silicon from Raman spectra. *J Appl Phys*. 2003;94(5):3582-3588. <https://doi.org/10.1063/1.1596364>
33. Finger F, Kroll U, Viret V, Shah A. Influences of a high excitation frequency (70 MHz) in the glow discharge technique on the process plasma and the properties of hydrogenated amorphous silicon. *J Appl Phys*. 1992;71(11):5665-5674. <https://doi.org/10.1063/1.350500>
34. Perrin J, Takeda Y, Hirano N, Takeuchi Y, Matsuda A. Sticking and recombination of the SiH₃ radical on hydrogenated amorphous

- silicon: the catalytic effect of diborane. *Surf Sci.* 1989;210(1-2):114-128. [https://doi.org/10.1016/0039-6028\(89\)90106-4](https://doi.org/10.1016/0039-6028(89)90106-4)
35. Richter H, Wang ZP, Ley L. The one phonon Raman spectrum in microcrystalline silicon. *Solid State Commun.* 1981;39(5):625-629. [https://doi.org/10.1016/0038-1098\(81\)90337-9](https://doi.org/10.1016/0038-1098(81)90337-9)
36. Haase F, Schafer S, Klamt C, et al. Perimeter recombination in 25%-efficient IBC solar cells with passivating POLO contacts for both polarities. *IEEE J Photovolt.* 2018;8(1):23-29. <https://doi.org/10.1109/JPHOTOV.2017.2762592>
37. Koida T, Ueno Y, Shibata H. In₂O₃-based transparent conducting oxide films with high electron mobility fabricated at low process temperatures. *Phys Status Solidi a.* 2018;215(7):1-14, 1700506. <https://doi.org/10.1002/pssa.201700506>
38. Dylla T, Reynolds S, Carius R, Finger F. Electron and hole transport in microcrystalline silicon solar cells studied by time-of-flight photocurrent spectroscopy. *J Non Cryst Solids.* 2006;352(9-20):1093-1096. <https://doi.org/10.1016/j.jnoncrysol.2005.12.015>
39. Bivour M, Reusch M, Schroer S, et al. Doped layer optimization for silicon heterojunctions by injection-level-dependent open-circuit voltage measurements. *IEEE J Photovolt.* 2014;4(2):566-574. <https://doi.org/10.1109/JPHOTOV.2013.2294757>
40. Cuevas A, Wan Y, Yan D, et al. Carrier population control and surface passivation in solar cells. *Sol Energy Mater sol Cells.* 2018;184:38-47. <https://doi.org/10.1016/j.solmat.2018.04.026>
41. Chavali RVK, De Wolf S, Alam MA. Device physics underlying silicon heterojunction and passivating-contact solar cells: a topical review. *Prog Photovolt Res Appl.* 2018;26(4):241-260. <https://doi.org/10.1002/pip.2959>
42. Procel P, Xu HY, Saez A, et al. The role of heterointerfaces and sub-gap energy states on transport mechanisms in silicon heterojunction solar cells. *Prog Photovolt Res Appl.* 2020;28(9):935-945. <https://doi.org/10.1002/pip.3300>
43. Pankove JI, Carlson DE, Berkeyheiser JE, Wance RO. Neutralization of shallow acceptor levels in silicon by atomic hydrogen. *Phys Rev Lett.* 1983;51:2224-2225. <https://doi.org/10.1103/PhysRevLett.51.2224>
44. Cuony P, Marending M, Alexander DTL, et al. Mixed-phase p-type silicon oxide containing silicon nanocrystals and its role in thin-film silicon solar cells. *Appl Phys Lett.* 2010;97(21):1-3, 213502. <https://doi.org/10.1063/1.3517492>
45. Coscia U, Ambrosone G, Lettieri S, et al. Preparation of microcrystalline silicon-carbon films. *Sol Energy Mater sol Cells.* 2005;87:433-444. <https://doi.org/10.1016/j.solmat.2004.09.015>
46. Takatsuka H, Noda M, Yonekura Y, Takeuchi Y, Yamauchi Y. Development of high efficiency large area silicon thin film modules using VHF-PECVD. *Solar Energy.* 2004;77:951-960. <https://doi.org/10.1016/j.solener.2004.06.007>

How to cite this article: Umishio H, Sai H, Koida T, Matsui T. Nanocrystalline-silicon hole contact layers enabling efficiency improvement of silicon heterojunction solar cells: Impact of nanostructure evolution on solar cell performance. *Prog Photovolt Res Appl.* 2021;29:344-356. <https://doi.org/10.1002/pip.3368>